

Indirectly regularized variational level set model for image segmentation

Yongfei Wu, Chuanjiang He*

College of Mathematics and Statistics, Chongqing University, Chongqing 401331, China

ARTICLE INFO

Article history:

Received 23 October 2014

Received in revised form

16 June 2015

Accepted 18 June 2015

Communicated by X. Gao

Available online 9 July 2015

Keywords:

Image segmentation

Level set

Variational model

Regularization

ABSTRACT

In this paper, we propose a variational level set model with indirect regularization term for image segmentation. Instead of using direct regularization on level set function, we introduce an auxiliary function to regularize indirectly the level set function. Our energy functional consists of a data term, a link term of level set function with the auxiliary function and a regularization term of the auxiliary function. We prove that the energy functional is convex in $L^2(\Omega) \times W^{1,2}(\Omega)$ and give the convergence analysis of the alternating minimization algorithm that we utilized. We show that the indirect regularization has some advantages over direct regularization theoretically and experimentally. Experimental results illustrate that the proposed model can better handle images with high noise, angle and weak edges.

© 2015 Elsevier B.V. All rights reserved.

1. Introduction

Image segmentation is an important subject in image processing and computer vision which facilitates the subsequent tasks such as image analysis, pattern recognition. Based on some similar characteristics (intensity value, texture, color) of the input image, one would like to partition the image domain into two or more regions, each representing an object. Up to now, a lot of good algorithms and methods have been proposed to address the image segmentation tasks.

Many successful approaches to image segmentation involve partial differential equations (PDE) and variational level set models. The evolution PDE for a PDE-based model is directly constructed or indirectly derived from a minimization problem, while the evolution PDE for a variational level set model is directly derived from the minimization of energy functional over level set functions. So far, there are a lot of researches for PDE-based models [1–7]. In this work, we focus on the variational level set methods for image segmentation.

Among a wealth of variational level set models [8–19], we must state the celebrated “active contours without edges” model proposed by Chan and Vese [8], one of the most widely used models for two-phase image segmentation. Its energy functional consists of two terms: a data term and a regularization term based on zero level set (i.e., length regularization). It works well in processing

images with a large amount of noise and can detect objects whose boundaries cannot be defined by gradient. But the Chan–Vese model has also the following limits.

First, it is difficult to handle images with intensity inhomogeneity because of its simple assumption of intensity homogeneity. To overcome this defect, many works [9–12] are proposed in different ways. These methods assume normally that the intensities are homogeneous in local regions of image. By dealing with image in terms of local regions instead of global regions, they perform well on images with intensity inhomogeneity. The popular methods include the well-known region-scalable fitting (RSF) model [9], the local image fitting (LIF) model [10], the local intensity clustering (LIC) model [11] and the local Gaussian intensity clustering (LGIC) model [12], etc.

Second, the minimizer of the energy functional for the Chan–Vese model [8] sometimes becomes a local one due to the non-convexity of functional. This is a serious difficulty because the local minima of functional often offer poor segmentation results. To overcome this difficulty, some researches [13–16] provided convex methods and algorithms to solve the non-convex problem of the Chan–Vese model. Chan et al. [13] provided an efficient global convex energy functional of the Chan–Vese (GCV) model to compute global minimizers by showing that solutions could be obtained from a convex relaxation, in which the total variation (TV) is used as the regularization term. Afterwards, Bresson et al. [14] proposed a global convex segmentation (GCS) model by integrating a weighted TV into the GCV model. Recently, Brown et al. [15] proposed a completely convex formulation of the Chan–Vese model, which is guaranteed to compute a global minimizer of functional under certain conditions. In our previous work [16], we proposed a convex variational level set model based on the coefficient of variation (CoV); we proved that the value of the

* Corresponding author.

E-mail addresses: yongfeiwu522@sina.com (Y. Wu), chuanjianghe@sina.com (C. He).

unique global minimizer for the energy functional is within the interval $[-1, 1]$ for any image, and equals to 1 in the object and -1 in the background for an ideal binary image.

Third, when implementing the Chan–Vese model, a re-initialization technique is usually needed periodically to maintain the degraded level set function being a signed distance function in the whole iteration process [8]. However, this regularization method is very time-consuming and introduces some fundamental problems about when and how to apply the re-initialization. To eliminate the re-initialization step, some variational level set formulations [20–23] have been proposed to regularize the level set function during evolution. These methods without re-initialization have many advantages over the traditional methods. The well-known distance regularization level set evolution (DRLSE) methods, including DRLSE1 [20], DRLSE2 [21] and DRLSE3 [22], keep the level set function as a signed distance function during the evolution. Recently, Zhang et al. [5] proposed a reaction–diffusion method for level set evolution by using the H^1 regularization, i.e., $E_R(\phi) = \int_{\Omega} |\nabla \phi|^2 dx$ where ϕ is the level set function. This method performs well on image with high noise because a standard method minimizing $E_R(\phi)$ is to find the steady-state solution of the gradient flow equation $\partial \phi / \partial t = \Delta \phi$. The role of this diffusion equation is to regularize the level set function ϕ ; it controls the smoothness of the zero level set to penalize complicated boundaries of regions and further avoid the occurrence of isolated small regions (e.g., noise points) in final segmentation. However, this processing is essentially equivalent to the Gaussian smoothing that will eventually output a constant function. At the meantime, some other shape-prior based level set methods [24,25] also reduce the re-initialization procedure by integrating a trained shape into the level set energy functional.

The aforementioned models can be categorized into the direct regularization framework, in which the regularization is directly posed on level set functions. In this paper, we propose an indirectly regularized variational level set model in which the regularization is posed indirectly on level set function via an auxiliary function. The energy functional of this model contains three terms: a data term, a link term of level set function with the auxiliary function and a regularization term of the auxiliary function. We prove that the proposed energy functional is convex in $L^2(\Omega) \times W^{1,2}(\Omega)$ and has a unique global minimizer. Since the energy functional is convex, the proposed model can be solved efficiently by means of the alternating minimization algorithm (see for example [26]). We show that the alternating minimization algorithm is convergent for the proposed model under mild conditions. Experiments on synthetic and real images illustrate that our model provides promising segmentation results compared with state-of-the-art works [5,8,13,16].

The organization of the remainder of this paper is as follows. In Section 2, we introduce some related works. In Section 3, we propose an indirectly regularized variational level set model and give a rigorous analysis. Section 4 gives the algorithm and convergence analysis. Section 5 presents experimental results. In Section 6, we discuss initializations of level set function and auxiliary function and the advantages of indirect regularization over direct regularization. This paper is summarized in Section 7.

2. Previous works

Let $\Omega \subset R^2$ be a bounded open connected set with a Lipschitz boundary, and $f : \Omega \rightarrow R$ be a given image. Let $\phi : \Omega \rightarrow R$ denote the level set function. Traditionally, the energy functional for the existing variational level set models can be formulated in the form:

$$E(\phi) = E_D(f, \phi) + E_R(\phi), \quad (1)$$

where $E_D(f, \phi)$ is the data term or external energy which makes the zero level set of ϕ deform so that it fits to the object boundary, and $E_R(\phi)$ is the regularization term or internal energy which penalizes the oscillation of ϕ .

2.1. About the data term

In [8], Chan and Vese constructed a data term which is expressed as the following formulation:

$$E_D(f, \phi) = \lambda_1 \int_{\Omega} (f - c_1)^2 H(\phi) dx + \lambda_2 \int_{\Omega} (f - c_2)^2 (1 - H(\phi)) dx, \quad (2)$$

where λ_1, λ_2 are positive parameters, and H is the Heaviside function. The constants c_1 and c_2 are defined as

$$c_1 = \frac{\int_{\Omega} f \cdot H(\phi) dx}{\int_{\Omega} H(\phi) dx}, \quad c_2 = \frac{\int_{\Omega} f \cdot (1 - H(\phi)) dx}{\int_{\Omega} (1 - H(\phi)) dx}, \quad (3)$$

which represent the mean intensity values of f in $\Omega_1 = \{x \in \Omega | \phi(x) > 0\}$ and $\Omega_2 = \{x \in \Omega | \phi(x) < 0\}$, respectively. The data term (2) is non-convex and so has sometimes local minima that often provide poor results.

To overcome this defect, Chan et al. [13] provided a convex relaxation method, in which the data term is defined as follows:

$$E_D(f, \phi) = \lambda \int_{\Omega} ((f - c_1)^2 - (f - c_2)^2) \phi dx, \quad \phi \in [0, 1], \quad (4)$$

where λ is a positive parameter, and the constants c_1 and c_2 are defined as

$$c_1 = \frac{\int_{\Omega_1} f(x) dx}{\int_{\Omega_1} dx}, \quad c_2 = \frac{\int_{\Omega_2} f(x) dx}{\int_{\Omega_2} dx}, \quad (5)$$

which represent the mean intensity values of f in $\Omega_1 = \{x \in \Omega | \phi(x) > \alpha\}$ and $\Omega_2 = \{x \in \Omega | \phi(x) < \alpha\}$ with $\alpha \in (0, 1)$, respectively. The energy functional in (4) is homogeneous of degree 1 with respect to ϕ , which does not exist minimizer in general, thus the authors simply restrict the values of ϕ such that $0 \leq \phi \leq 1$.

Recently, Lee and Seo [17] proposed the following data term with two shifted Heaviside functions:

$$E_D(f, \phi) = \lambda_1 \int_{\Omega} (f - c_1)^2 \phi H(\alpha + \phi) dx - \lambda_2 \int_{\Omega} (f - c_2)^2 \phi H(\alpha - \phi) dx, \quad (6)$$

where λ_1, λ_2 are positive parameters, and α is an arbitrary positive value. Here, ϕ is multiplied to prevent from computing a local minimum and $H(\pm \phi)$ is shifted by $\mp \alpha$ to confine the range of ϕ . As is the case for the formulation (2), the two constants c_1 and c_2 in (6) are still defined by (3). The Lee–Seo model has a global minimum, and so works well on two-phase image segmentation problems. Based on the Lee–Seo model, Li and Kim [18] replace the Heaviside function in the Lee–Seo model with the function:

$$H_c(z) = \frac{1+z}{2}, \quad (7)$$

and get the following data term:

$$E_D(f, \phi) = \lambda_1 \int_{\Omega} (f - c_1)^2 \phi H_c(1 + \phi) dx - \lambda_2 \int_{\Omega} (f - c_2)^2 \phi H_c(1 - \phi) dx, \quad (8)$$

The constants c_1 and c_2 are defined as

$$c_1 = \frac{\int_{\Omega} f \cdot H_c(\phi) dx}{\int_{\Omega} H_c(\phi) dx}, \quad c_2 = \frac{\int_{\Omega} f \cdot (1 - H_c(\phi)) dx}{\int_{\Omega} (1 - H_c(\phi)) dx}. \quad (9)$$

The Li–Kim model can be numerically solved using an unconditionally stable semi-implicit scheme and segments well two-phase images.

In our previous work [16], we proposed a convex data term based on CoV (coefficient of variation), given by

$$E_D(f, \phi) = \lambda \int_{\Omega} \frac{(f - c_1)^2}{c_1^2} (\phi + 1)^2 dx + \int_{\Omega} \frac{(f - c_2)^2}{c_2^2} (\phi - 1)^2 dx, \quad (10)$$

where λ is a positive parameter, and the constants c_1 and c_2 are defined as

$$c_1 = \frac{\int_{\Omega} f^2 \cdot H(\phi) dx}{\int_{\Omega} f \cdot H(\phi) dx}, \quad c_2 = \frac{\int_{\Omega} f^2 \cdot (1 - H(\phi)) dx}{\int_{\Omega} f \cdot (1 - H(\phi)) dx}. \quad (11)$$

We have proved that the values of the unique global minimizer for the data term (10) are within the interval $[-1, 1]$ for any image, and equal to 1 in the object and -1 in the background for an ideal binary image.

2.2. About the regularization term

In implementing variational level set evolution, the level set function needs to be regularized in order to prevent the oscillation of ϕ . For example, in [8], Chan and Vese utilized the length regularization term which is defined as

$$E_R(\phi) = \int_{\Omega} |\nabla H(\phi)| dx. \quad (12)$$

Besides, the re-initialization procedure usually needs be performed periodically during the evolution to reshape the degraded level set function as a signed distance function. However, the re-initialization procedure brings some fundamental problems such as when and how to apply the re-initialization.

To avoid re-initialization procedure of traditional level set methods, Li et al. [20] proposed the following distance regularization term:

$$E_R(\phi) = \int_{\Omega} (|\nabla \phi| - 1)^2 dx, \quad (13)$$

which is used to constrain the level set function to be a signed distance function. This regularization term can be integrated into various variational level set models [9,11,12]. However, this regularization term may cause some undesirable side effects (such as numerical instability) in some situations. Afterwards, they proposed the improved distance regularization term [21]:

$$E_R(\phi) = \begin{cases} \int_{\Omega} (|\nabla \phi| - 1)^2 dx, & |\nabla \phi| \geq 1 \\ \int_{\Omega} \frac{1}{(2\pi)^2} (1 - \cos(2\pi|\nabla \phi|)) dx, & |\nabla \phi| \leq 1 \end{cases} \quad (14)$$

In [22], Xie proposed the following regularization term:

$$E_R(\phi) = \int_{\Omega} H_\epsilon(|\nabla \phi| - 1) dx. \quad (15)$$

where $H_\epsilon(z) = (1/2)[1 + (2/\pi)\arctan(z/\epsilon)]$ and ϵ is a fixed parameter. The two regularization terms alleviate the oscillation of level set function but increases the time consumption.

In [2], Zhang et al. proposed a Gaussian regularized level set evolution method based on the equation:

$$\frac{\partial \phi}{\partial t} = \Delta \phi, \quad (16)$$

which is the gradient descent flow of the regularization term:

$$E_R(\phi) = \frac{1}{2} \int_{\Omega} |\nabla \phi|^2 dx. \quad (17)$$

The evolution by Eq. (16) is essentially equivalent to the Gaussian smoothing, so the re-initialization procedure can be eliminated during the evolution.

3. The proposed model

Our energy functional is composed of a data term, a link term of level set function and an auxiliary function, and a regularization term of the auxiliary function:

$$E(\phi, \psi) = E_D(f, \phi) + E_L(\phi, \psi) + E_R(\psi). \quad (18)$$

The first term in (18) is the data term, which aims to separate the object from the background. Based on our previous work [16], the data term is defined as

$$E_D(f, \phi) = \lambda_1 \int_{\Omega} (f - c_1)^2 (\phi + 1)^2 dx + \lambda_2 \int_{\Omega} (f - c_2)^2 (\phi - 1)^2 dx, \quad (19)$$

where the constants c_1 and c_2 are given by

$$c_1 = \frac{\int_{\Omega} f \cdot (\phi + 1)^2 dx}{\int_{\Omega} (\phi + 1)^2 dx}, \quad c_2 = \frac{\int_{\Omega} f \cdot (\phi - 1)^2 dx}{\int_{\Omega} (\phi - 1)^2 dx}, \quad (20)$$

which are obtained by minimizing the data term $E_D(f, \phi)$ with respect to c_1 and c_2 for fixed ϕ .

The second term in (18) is the link term, connecting the first term and the third term in (18). The link term guarantees that the level set function ϕ cannot be far away from the auxiliary function ψ in the iterative process. In this study, the link term is chosen as $E_L(\phi, \psi) = \mu \int_{\Omega} (\phi - \psi)^2 dx$, which measures the similarity of the level set function ϕ and the auxiliary function ψ .

The last term in (18) aims to regularize the auxiliary function ψ , which penalizes indirectly the oscillation of the level set function ϕ by the link term $E_L(\phi, \psi)$. This regularization term is properly chosen depending upon different regularization demands; it has typically the following forms:

- Length regularization: $E_R(\psi) = \nu \int_{\Omega} |\nabla H(\psi)| dx$, e.g. [8,9,11].
- TV regularization: $E_R(\psi) = \nu \int_{\Omega} |\nabla \psi| dx$, e.g. [13–15].
- H^1 -regularization: $E_R(\psi) = \nu \int_{\Omega} |\nabla \psi|^2 dx$, e.g. [5].

In this study, the regularization term is chosen as $E_R(\psi) = \nu \int_{\Omega} |\nabla \psi|^2 dx$. Because the minimization of $E_R(\psi)$ is equivalent to finding the steady state solution of the gradient flow equation $\partial \psi / \partial t = \mu \Delta \psi$, the H^1 -regularization can be more robust to high noise than the length and TV regularizations. In Fig. 1, we give the experimental results to test the robustness of the data and link terms

$$E_D(f, \phi) + E_L(\phi, \psi) = \lambda_1 \int_{\Omega} (f - c_1)^2 (\phi + 1)^2 dx + \lambda_2 \int_{\Omega} (f - c_2)^2 (\phi - 1)^2 dx + \mu \int_{\Omega} (\phi - \psi)^2 dx \quad (21)$$

with one of the above three regularizations to high noise. The first row of Fig. 1 illustrates five images with the same object, in which the first image is noise-free and the last four noisy images were generated by adding Gaussian noises (zero mean, variances 0.001, 0.005, 0.01 and 0.05) to the first noise-free image, respectively. The corresponding segmentation results are shown in the second row (length regularization), the third row (TV regularization) and the last row (H^1 -regularization). Both the length and TV regularizations can extract the object accurately when the noise is very low, as shown in the first two columns of Fig. 1. However, they perform poor when encountering high noise; see the last three columns of Fig. 1. Conversely, the H^1 -regularization extracts the object acceptably even when the noise is very high; see the last row of Fig. 1.

The proposed model is thus defined as

$$E(c_1, c_2, \phi, \psi) = \lambda_1 \int_{\Omega} (f - c_1)^2 (\phi + 1)^2 dx + \lambda_2 \int_{\Omega} (f - c_2)^2 (\phi - 1)^2 dx$$

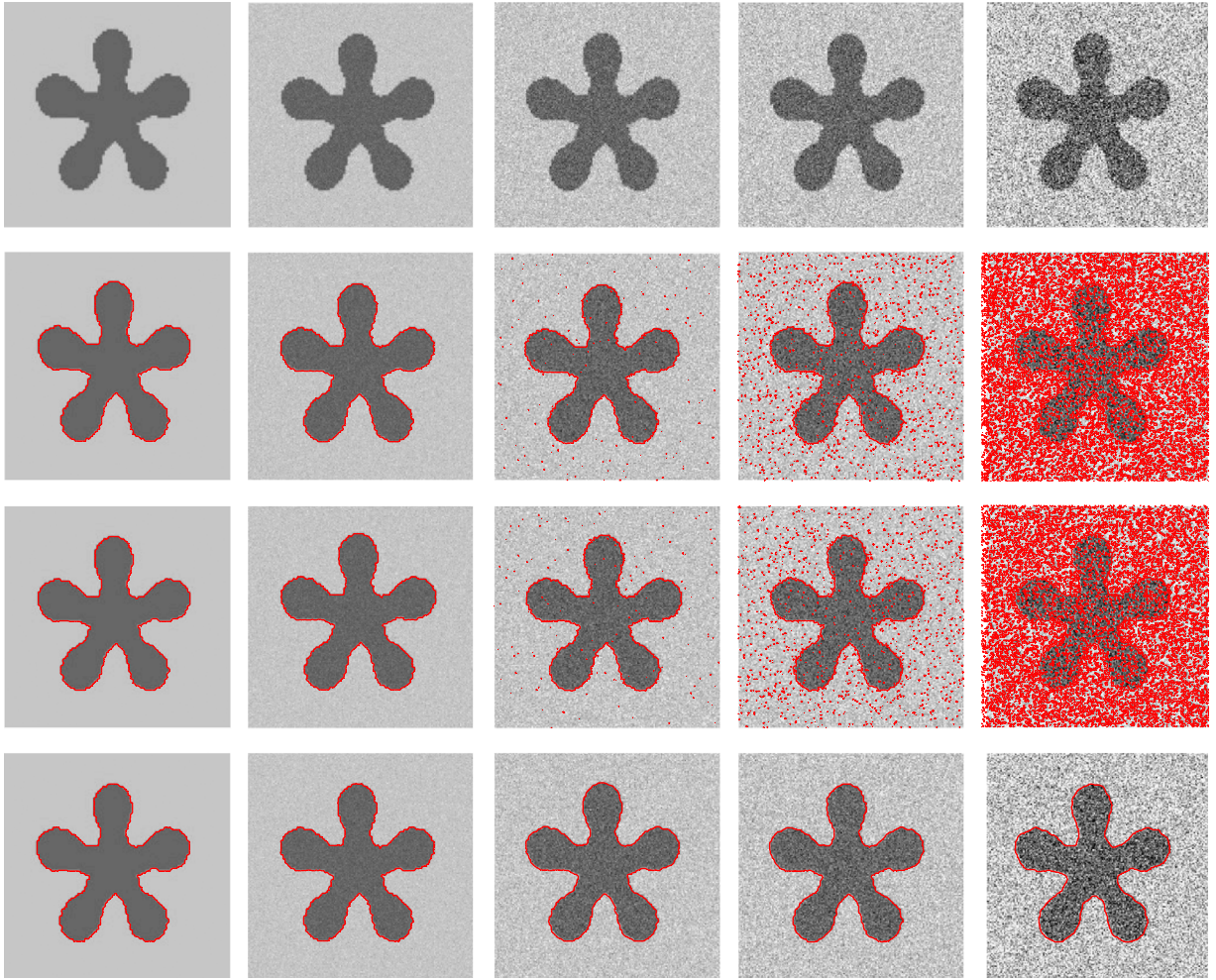


Fig. 1. Segmentation results of the data and link terms (21) with one of the three regularizations. First row: original images (left to right: noise-free image, Gaussian noisy images (zero mean, variances 0.001, 0.005, 0.01 and 0.05). Second row: with length regularization. Third row: with TV regularization. Last row: with H^1 regularization.

$$+\mu \int_{\Omega} (\phi - \psi)^2 dx + \nu \int_{\Omega} |\nabla \psi|^2 dx, \quad (22)$$

where $\lambda_1, \lambda_2, \mu$ and ν are positive parameters, and $\phi \in L^2(\Omega)$, $\psi \in W^{1,2}(\Omega)$ (Sobolev space).

In what follows, we discuss the properties of the energy functional in (22).

Theorem 1. Let $f \in L^2(\Omega)$, then the energy functional in (22) is strictly convex in $L^2(\Omega) \times W^{1,2}(\Omega)$ for any fixed constants c_1, c_2 .

Proof. See Appendix A.

Theorem 2. Let $f \in L^2(\Omega)$. The energy functional in (22) has a unique minimizer $\phi^* \in L^2(\Omega)$ for fixed c_1, c_2 and ψ , while it has a unique minimizer $\psi^* \in W^{1,2}(\Omega)$ for fixed c_1, c_2 and ϕ .

Proof. See Appendix A.

4. Algorithm and convergence analysis

4.1. The AM algorithm

The above theorems guarantee that the proposed model has a unique global minimizer of one variable with the other variables fixed. Here, we present an efficient algorithm based on alternating

minimization (AM) (see for example [26]) to solve the proposed model. The main steps of the algorithm are as follows:

Step 1. Find c_1 and c_2 as the minimizer of (22) for fixed ϕ and ψ . They are given by (see (20)):

$$c_1 = \frac{\int_{\Omega} f \cdot (\phi+1)^2 dx}{\int_{\Omega} (\phi+1)^2 dx}, \quad c_2 = \frac{\int_{\Omega} f \cdot (\phi-1)^2 dx}{\int_{\Omega} (\phi-1)^2 dx}. \quad (23)$$

Step 2. Find ϕ as the minimizer of (22) for fixed c_1, c_2 and ψ . It is directly deduced that

$$\phi = \left(\mu + \lambda_1(f - c_1)^2 + \lambda_2(f - c_2)^2 \right)^{-1} \left(\mu\psi - \lambda_1(f - c_1)^2 + \lambda_2(f - c_2)^2 \right). \quad (24)$$

Step 3. Find ψ as the minimizer of (22) for fixed c_1, c_2 and ϕ . Its Euler–Lagrange equation is as follows:

$$(-\nu \Delta + \mu)\psi = \mu\phi. \quad (25)$$

This equation can be solved efficiently by the Fast Fourier Transform (FFT) (see for example [28,29]) or other classical stationary iterative methods such as the Gauss–Seidel method. In

this work, we apply FFT and obtain the closed-form solution of ψ by

$$\psi = \mathcal{F}^{-1} \left(\frac{\mu \mathcal{F} \phi}{\mu - \nu (\mathcal{F}^*(\nabla_x) \mathcal{F}(\nabla_x) + \mathcal{F}^*(\nabla_y) \mathcal{F}(\nabla_y))} \right), \quad (26)$$

where \mathcal{F} is the Fourier transform, \mathcal{F}^* denotes complex conjugate of \mathcal{F} , ∇_x and ∇_y are difference operators in x -coordinate and y -coordinate, respectively.

In summary, the minimization of the energy functional (22) can be solved approximately by the following algorithm.

Algorithm 1.

Input: ϕ^0 and ψ^0 .

For $k = 0, 1, 2, \dots$ do

 find c_1^{k+1} and c_2^{k+1} as minimizer of (22) for fixed ϕ^k and ψ^k using (23);

 find ϕ^{k+1} as minimizer of (22) for fixed c_1^{k+1} , c_2^{k+1} and ψ^k using (24);

 find ψ^{k+1} as minimizer of (22) for fixed c_1^{k+1} , c_2^{k+1} and ϕ^{k+1} using (26);

end For

4.2. Convergence analysis

Following [30], we investigate the convergence of Algorithm I. For convenience, we set $c = (c_1, c_2)$. To proceed the algorithm, starting with some initial guesses ϕ^0 and ψ^0 , we successively gets the alternating sequence:

$$\phi^0, \psi^0 \rightarrow c^0 \rightarrow \phi^1 \rightarrow \psi^1 \rightarrow c^1 \rightarrow \dots$$

by solving, for $k = 0, 1, \dots$,

$$c^k = \arg \min_c E(c, \phi^k, \psi^k),$$

$$\phi^{k+1} = \arg \min_{\phi} E(c^k, \phi, \psi^k),$$

$$\psi^{k+1} = \arg \min_{\psi} E(c^k, \phi^{k+1}, \psi). \quad (27)$$

Theorem 3. For each $k \geq 0$, we have for the energy functional (22):

$$E(c^k, \phi^{k+1}, \psi^{k+1}) \leq E(c^{k-1}, \phi^k, \psi^k),$$

$$E(c^k, \phi^{k+1}, \psi^k) \leq E(c^{k-1}, \phi^k, \psi^{k-1}),$$

$$E(c^{k+1}, \phi^{k+1}, \psi^{k+1}) \leq E(c^k, \phi^k, \psi^k).$$

Hence, the sequence $\{E(c^k, \phi^k, \psi^k)\}_{k \in \mathbb{N}}$ converges monotonically.

Proof. See Appendix A.

Theorem 4. Let $(c^k, \phi^k, \psi^k)_{k \in \mathbb{N}}$ is a convergent sequence generated from (27):

$$(c^k, \phi^k, \psi^k) \rightarrow (c^*, \phi^*, \psi^*) \text{ as } k \rightarrow \infty \text{ in } \mathbb{R}^2 \times L^2(\Omega) \times W^{1,2}(\Omega)$$

Then the limit (c^*, ϕ^*, ψ^*) must satisfy

$$E(c^*, \phi^*, \psi^*) \leq E(c, \phi^*, \psi^*), \quad \forall c \in \mathbb{R}^2,$$

$$E(c^*, \phi^*, \psi^*) \leq E(c^*, \phi, \psi^*), \quad \forall \phi \in L^2(\Omega),$$

$$E(c^*, \phi^*, \psi^*) \leq E(c^*, \phi^*, \psi), \quad \forall \psi \in W^{1,2}(\Omega).$$

Proof. See Appendix A.

5. Experimental results

In this section, the proposed model is tested on various synthetic and real images from different modalities and compared with the CV model [8], the GCV model [13], the RD model [5] and the GCoV model [16]. The two functions ϕ and ψ are always simply initialized to the same constant function (i.e., $\phi^0 = \psi^0 = 0.5$) for all experiments. Unless otherwise specified, we use the following default setting of the parameters for all the experiments: $\lambda_1 = 1$, $\lambda_2 = 1$, $\mu = 1$ and $\nu = 1$.

We first validate visually the capability of the proposed model to handle noise. The test images are three images with high noise, which are shown in the top row of Fig. 2. The segmentation results are demonstrated in the bottom row of Fig. 2. We observe that the proposed model segments all these noisy images well.

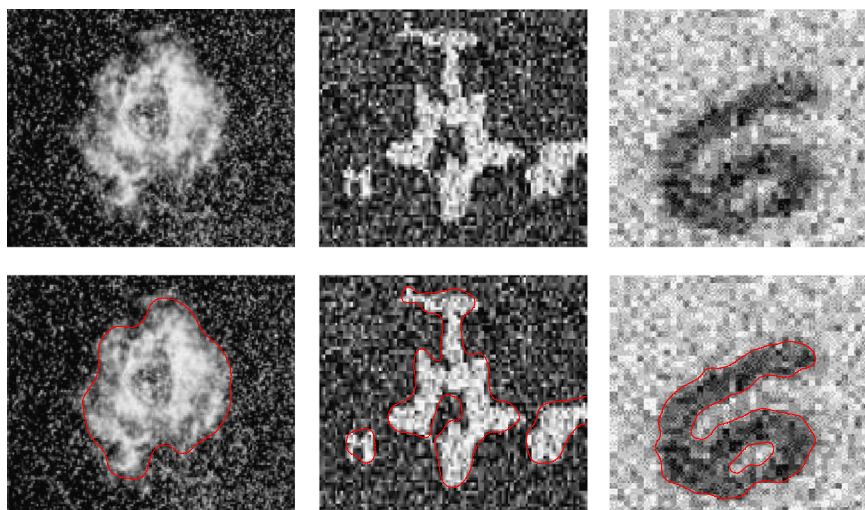


Fig. 2. Segmentation results of the proposed model for three images with high noise. Top row: original images. Bottom row: corresponding segmentation results.

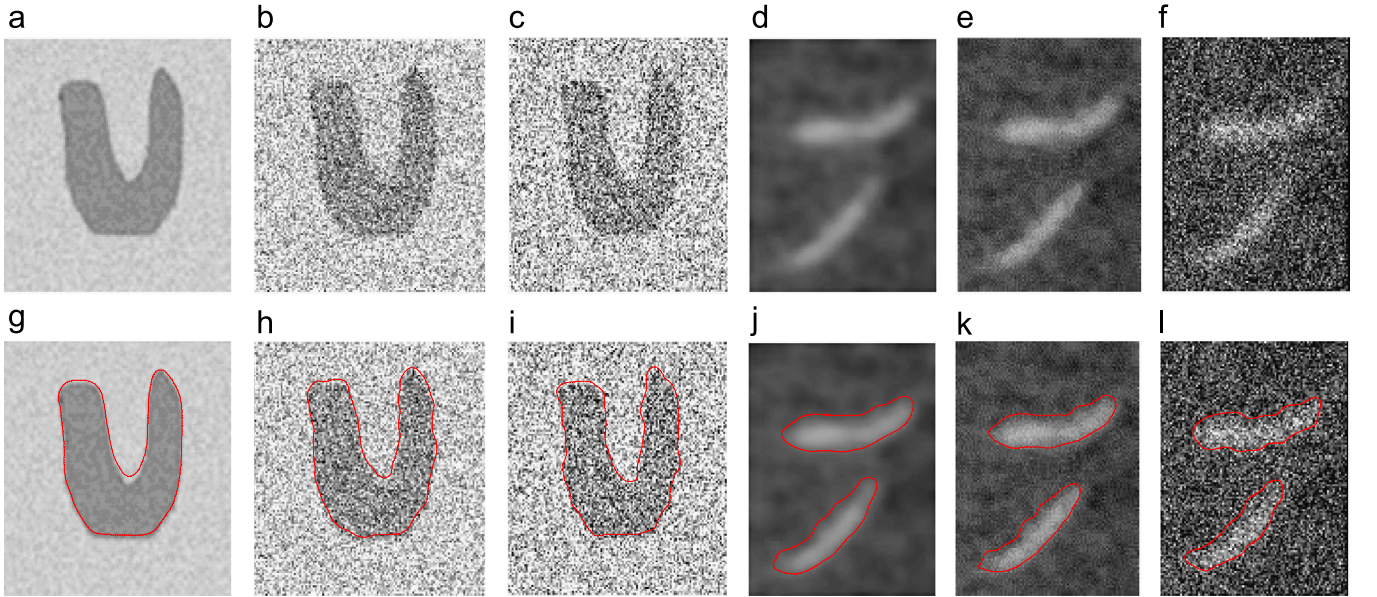


Fig. 3. Segmentation results of the proposed model for three images with and without (Gaussian) noise. (a) And (d) original images; (b) and (e) noisy images (zero mean, 0.05 variance); (c) and (f) noisy images (zero mean, 0.1 variance). (g)–(l) corresponding segmentation results.

We then evaluate quantitatively the robustness of our model to noise according to four quantitative metrics. The four metrics are the False Positive Ratio (FPR) and the False Negative Ratio (FNR) [31], the Ratio of Segmentation Error (RSE) [32] and the Dice Similarity Coefficient (DSC) [33]. Let R_1 and R_2 represent a given baseline foreground region (e.g., true object) and the foreground region obtained by the proposed model, respectively. Then these four metrics are defined as

$$\begin{aligned} FPR &= \frac{N(R_2 \setminus R_1)}{N(R_2)}, \quad FNR = \frac{N(R_1 \setminus R_2)}{N(R_1)} \\ RSE &= \frac{N(R_2 \setminus R_1) + N(R_1 \setminus R_2)}{N(\Omega)}, \quad DSC = \frac{2N(R_1 \cap R_2)}{N(R_1) + N(R_2)} \end{aligned}$$

where $N(\cdot)$ represents the number of pixels in the corresponding region. A perfect segmentation will give $FPR = FNR = RSE = 0$ and $DSC = 1$.

The test images are chosen as a synthetic image and a real vascular biopsy image which are shown in Fig. 3(a and d), respectively. The corresponding segmentation results by the proposed model are served as ground truth foreground regions; see Fig. 3(g and j). Then, we generate four noisy images by adding Gaussian noise (zero mean, variances 0.05 and 0.1) into the two test images. The four noisy images are shown in Fig. 3(b, c, e and f). From the bottom row of Fig. 3, it can be observed that our model segments successfully all objects in these noisy images and obtains similar visual quality for the original and noisy images. Furthermore, the quantitative metric values listed in Table 1 show that our model really produces the perfect results for these noisy images.

In the following three experiments (Figs. 4–6), we give the comparisons of the proposed model with four models (CV model [8], GCV model [13], RD model [5] and GCoV model [16]).

In Fig. 4, we compare our model with four models for segmenting real digital mammography images. The goal is to extract the tumors from the background. The tumors typically appear more brightly than the background in the mammography. However, intensities of some tumors and/or their parts are very close to their background and the boundaries are very blurry. As shown in Fig. 4, the CV model failed to segment all four images. While the other three models perform slightly better than the CV model, but do not extract the object boundary completely. On the contrary, our model obtains satisfactory results for all four images.

Table 1
The four metric values for the images in Fig. 3.

Image ID	(h)	(i)	(k)	(l)
FPR	0.0098	0.0132	0.0172	0.0372
FNR	0.0051	0.0101	0.0066	0.0078
RSE	0.0073	0.0047	0.0180	0.0502
DSC	0.9976	0.9985	0.9946	0.9849

Fig. 5 shows segmentation results of five models for real skin lesion images which are taken from Science Photo Library (<http://www.sciencephoto.com>). Extracting lesion regions from background is a basic step in computer-aided lesion analysis. However, due to the presence of high noise, or complex background, or blurry boundaries, it becomes more difficult to obtain accurate segmentation results. The second column shows that the CV model failed to extract object accurately due to interference of high noise. The third and fourth columns show that the GCV model and the RD model perform better than the CV model because they utilize effective regularization methods. The fifth column shows that the GCoV model can locate the object boundary but emerging some small contours (because it involves no regularization). However, we observe from the last column of Fig. 5 that our model gets satisfactory segmentation results for all these images.

In Fig. 6, we compared our method with the same four models for segmenting real brain CT images. We give three test CT images with irregular white matter boundary and weak boundary in the first column of Fig. 6. As demonstrated in Fig. 6, the CV model, the GCV model and the RD model have not extract the white matter boundary successfully, while the GCoV model performs well than the above three models but does not locate the white tissue boundary completely. In contrast, the proposed model extracts the white tissue in these images successfully and accurately.

In Fig. 7, we evaluate the efficiency of our model by comparing with four models in terms of iteration numbers and CPU time. Three synthetic images are chosen as test data, for which the four models and our model can all yield satisfied results. We tune the parameters for the four test models so that they return the best segmentation results. The comparison results are illustrated in Table 2. It can be seen that our model achieves better performance in terms of both iteration numbers and CPU time, although it

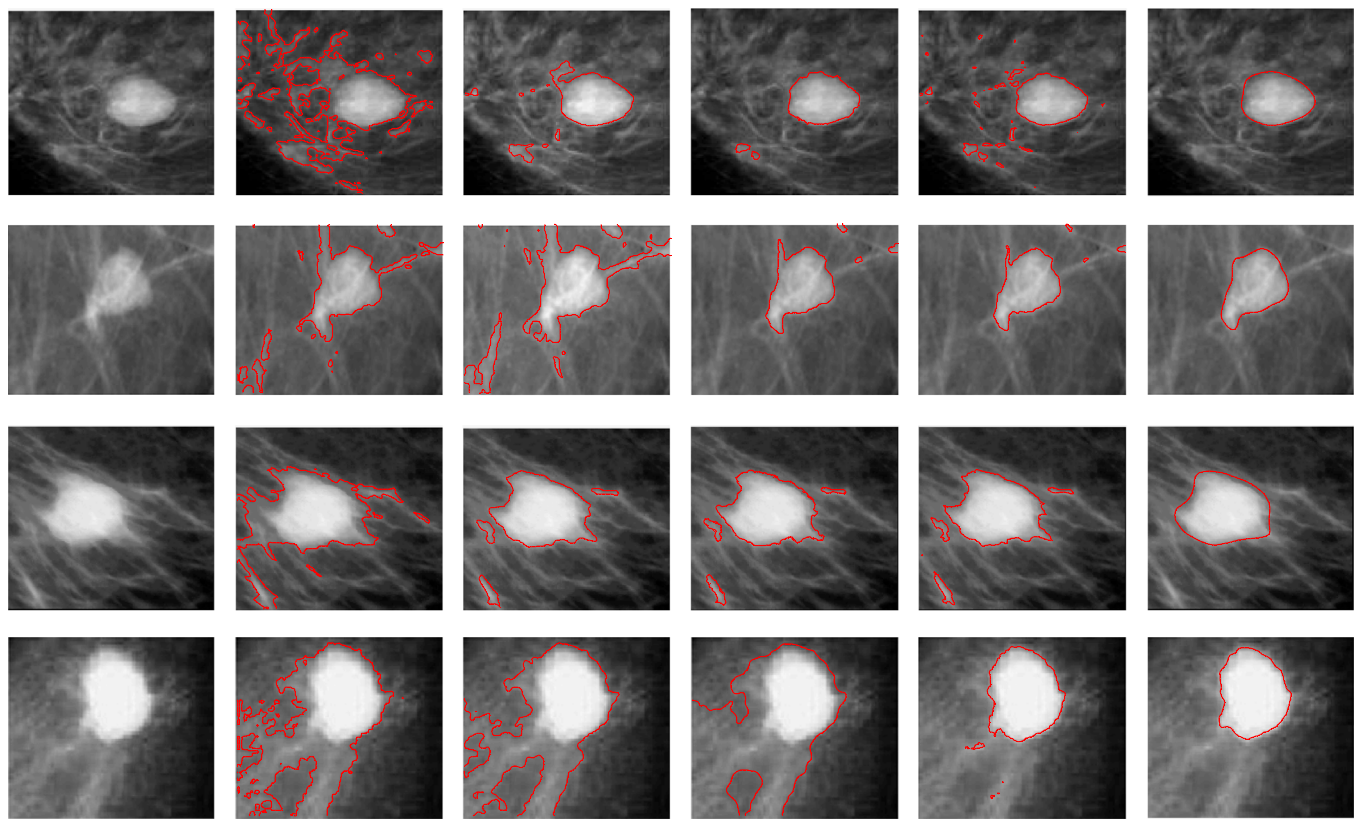


Fig. 4. Segmentation results of five models for digital mammography images. The first column: original images; the second to sixth columns: segmentation results of CV, GCV, RD, GCoV and ours, respectively.

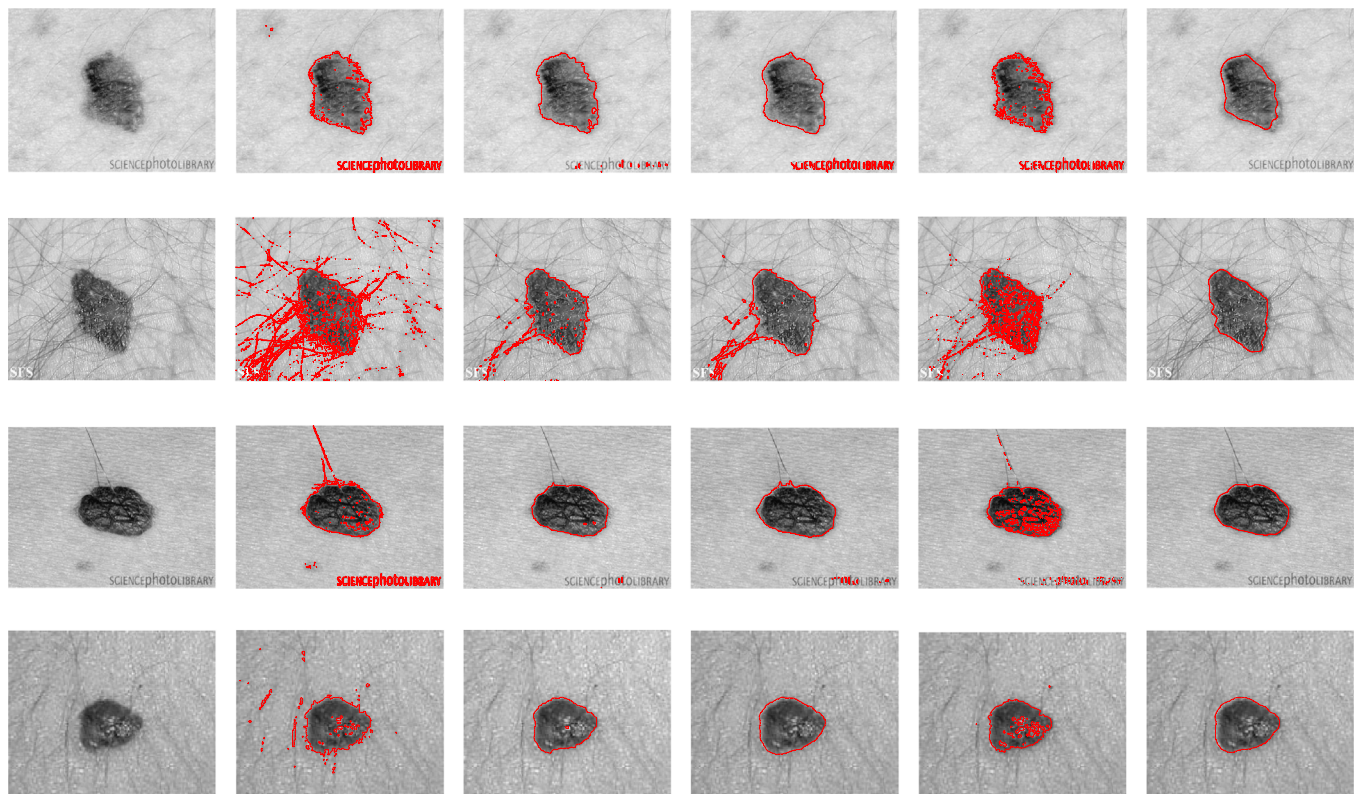


Fig. 5. Segmentation results of five models for skin lesion images. The first column: original images; the second to sixth columns: segmentation results of CV, GCV, RD, GCoV and ours, respectively.

involves the burden of the FFT computation about the auxiliary function.

Next, we further test the performance of the proposed method for eight two-phase images from Berkeley Image Segmentation Dataset [34]. These test images are converted into gray scale images in our experiments. The segmentation results are shown in Fig. 8, from which we can observe that the proposed method performs well on these nature images.

It should be pointed out that the data term of our model is simply based on the image intensity. If the intensity distribution of the object involves local statistical information such as complex textures, the proposed model fails to segment the objects from images, as shown in Fig. 9.

6. Discussions

6.1. Initializations of level set function and auxiliary function

For the proposed model with Algorithm I, we need to initialize the level set function ϕ and the auxiliary function ψ . In this section, we

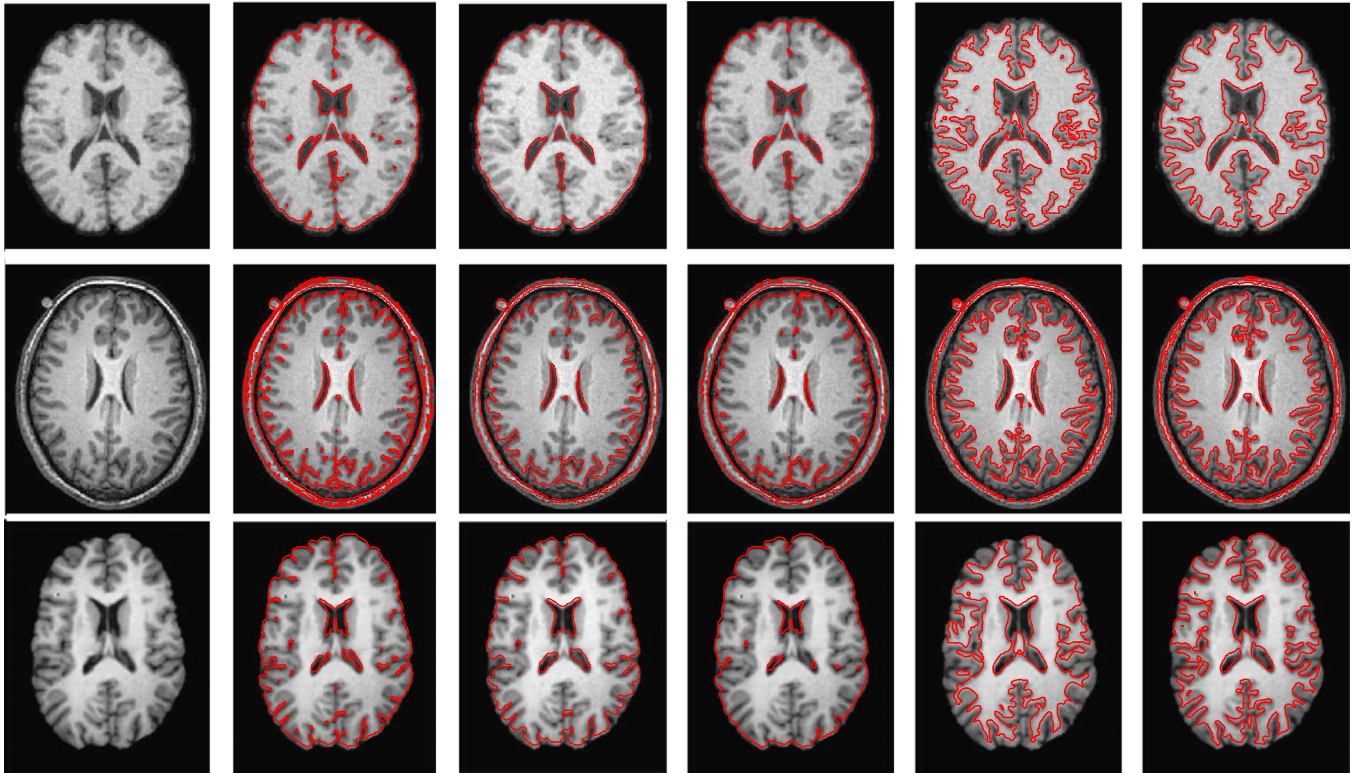


Fig. 6. Segmentation results of five models for three real brain CT images. The first column: original images; the second to sixth columns: segmentation results of CV, GCV, RD, GCoV and ours, respectively.

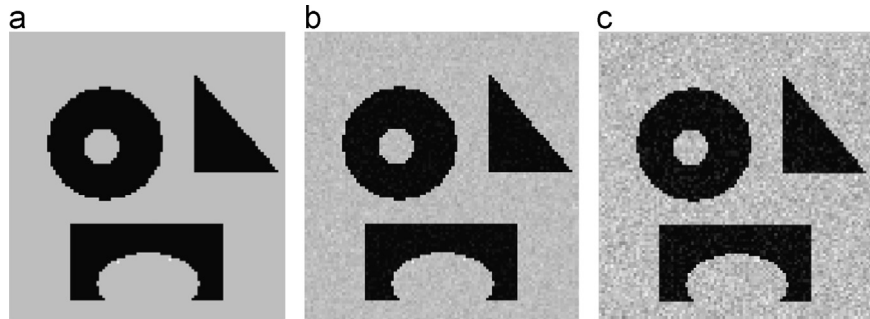


Fig. 7. (a) Noise-free image; (b) Gaussian noisy image (zero mean and variance 0.001); (c) Gaussian noisy image (zero mean and variance 0.005).

verify experimentally that our model can obtain the same zero level set of ϕ in the steady state, starting with any initial functions $\phi^0 \in L^2(\Omega)$ and $\psi^0 \in W^{1,2}(\Omega)$. For simplicity, we set $\psi^0 = \phi^0$.

Here, we list the initial level set functions that usually used in variational level set models as follows:

1. Sign distance function [8]:

$$\phi(x) = \begin{cases} \pm d(x, C) & x \in \text{inside}(C) \\ 0 & x \in C \\ \mp d(x, C) & x \in \text{outside}(C) \end{cases}, \quad (28)$$

where $d(x, C)$ denotes the (shortest) Euclidean distance from the point x to contour C .

2. Binary step function [4,9]:

$$\phi(x) = \begin{cases} \pm \rho & x \in \omega \\ \mp \rho & x \in \Omega \setminus \omega \end{cases}, \quad (29)$$

where $\rho \neq 0$ is constant, and ω is a subset in the image domain Ω . The subset ω is typically defined by a closed curve (e.g., circle or square) [9], or a line segment that partitions the image domain Ω into two disjoint regions [4].

3. Constant function [3,16]:

$$\phi(x) = \pm \rho \quad x \in \Omega, \quad (30)$$

where $\rho \neq 0$ is constant.

Table 2

Comparison of segmentation efficiency by five models for three images shown in Fig. 7.

Image	<i>a</i>		<i>b</i>		<i>c</i>	
	Time(s)	Iter	Time(s)	Iter	Time(s)	Iter
CV	3.0	150	4.9	250	7.5	400
GCV	0.6	10	0.7	15	0.8	20
RD	0.9	30	1.8	70	2.3	100
GCoV	0.3	5	0.8	10	2.7	90
Ours	0.3	9	0.5	10	0.5	10

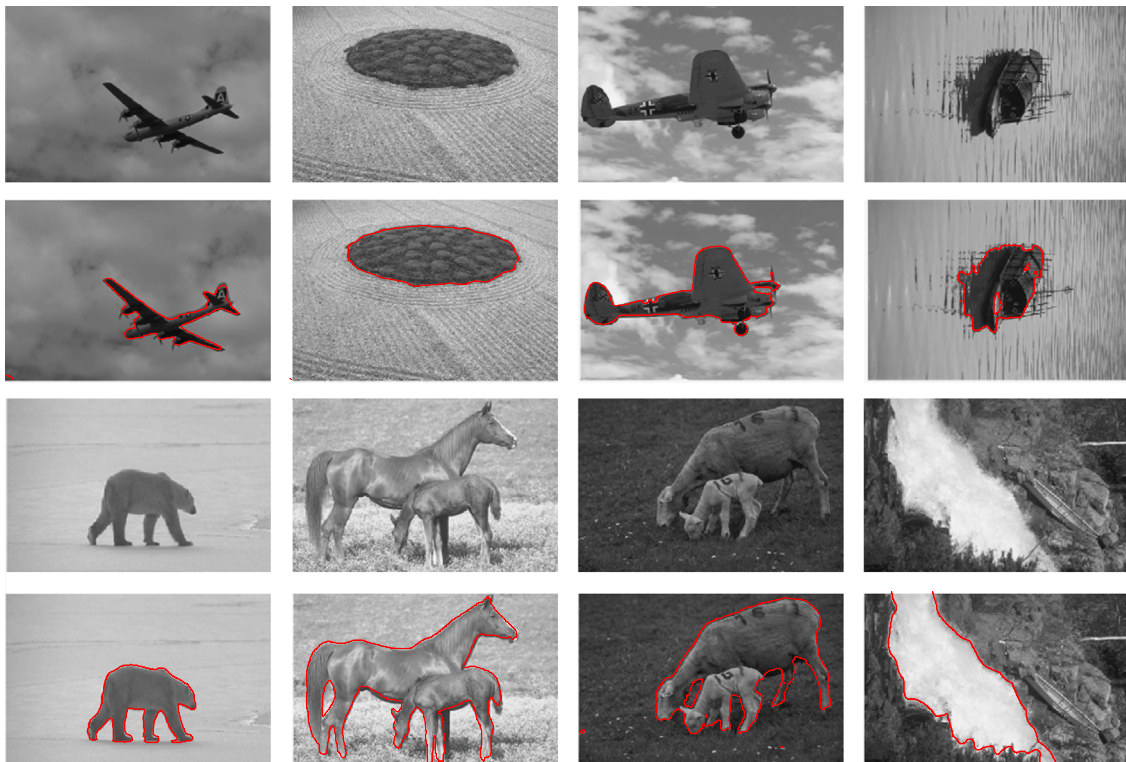


Fig. 8. Segmentation results of the proposed model for eight two-phase images from Berkeley Image Segmentation Dataset. First and third rows: original images. Second and fourth rows: segmentation results.

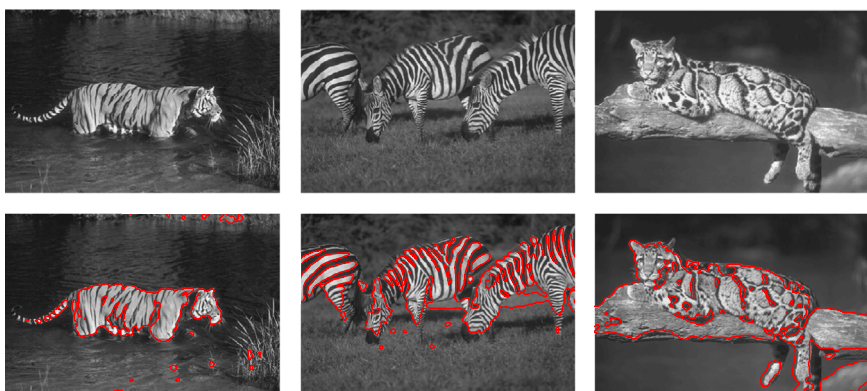


Fig. 9. The proposed model fails to segment images with complex textures. Top row: original images. Bottom row: segmentation results of the proposed model.

In Fig. 10, we give a simple experiment on a noisy image, starting with one of the four initial functions (constant, signed distance, binary step functions defined respectively by a square and a line). The first, second, third and fourth rows in Fig. 10 show the iterative process of the zero level set of ϕ with initial value ϕ^0 , where ϕ^0 is a constant, signed distance and two binary step functions, respectively. In Fig. 10, the contours are all overlaid on the original images. In each case, all these different initializations give really the same final contour (see the last column of Fig. 10). We also tested on other images; our observation is that the same segmentation result can be obtained regardless of which of the four different initializations.

6.2. Advantages of indirect regularization

Unlike the existing models, the proposed model can be categorized into the indirect regularization framework. In order to show the advantages of indirect regularization over direct one, we

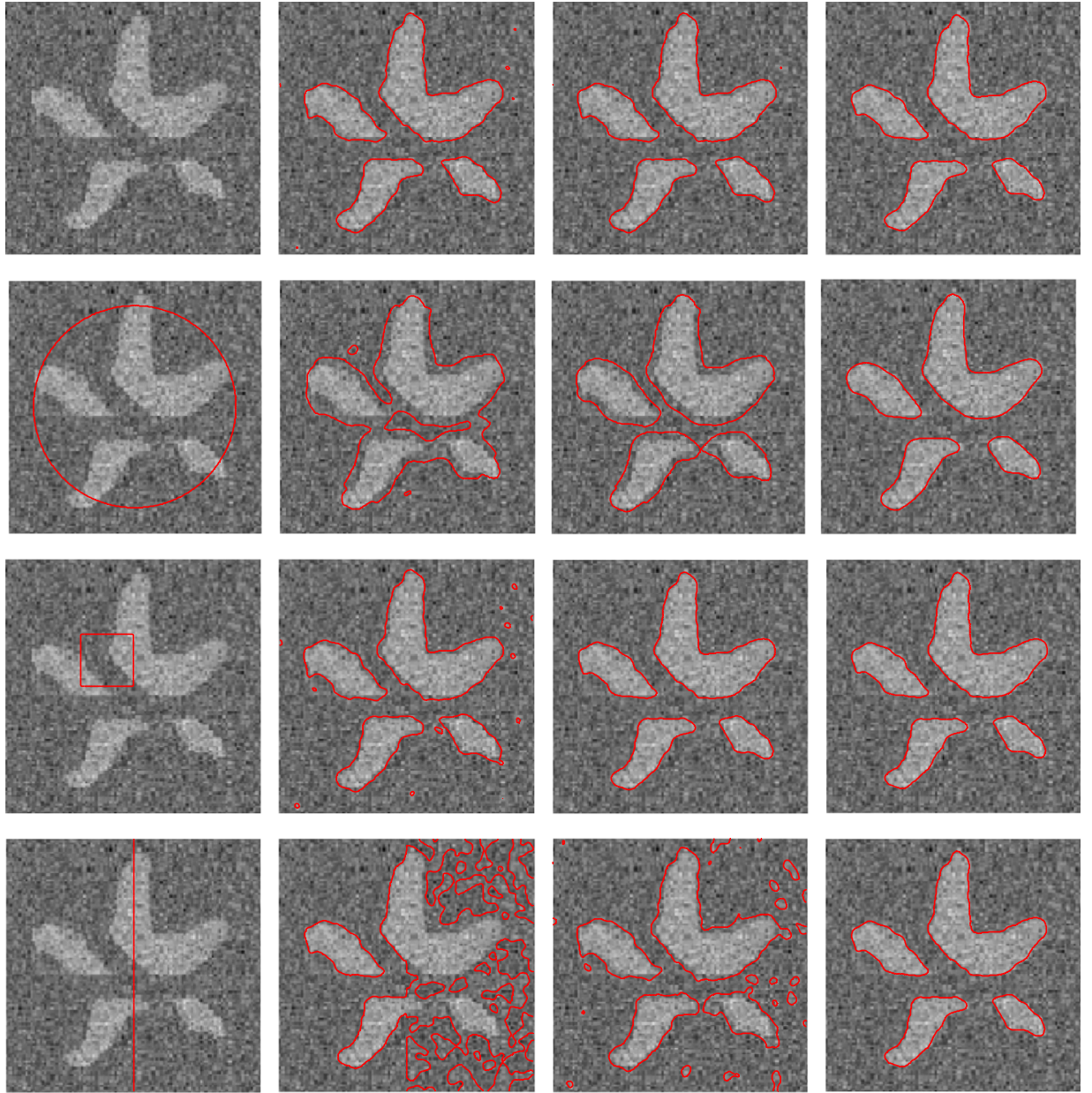


Fig. 10. Segmentation results of our model with four initial functions for a noisy image. First column: initial contours superimposed on the original images. Second column: contours after two iterations. Third column: contours after four iterations. Last column: contours after 20 iterations.

first present the following model with direct regularization:

$$\begin{aligned} E_{\text{direct}}(c_1, c_2, \phi) &= E_D(f, \phi) + E_R(\phi) \\ &= \lambda_1 \int_{\Omega} (f - c_1)^2 (\phi + 1)^2 dx \\ &\quad + \lambda_2 \int_{\Omega} (f - c_2)^2 (\phi - 1)^2 dx \\ &\quad + \nu \int_{\Omega} |\nabla \phi|^2 dx, \end{aligned} \quad (31)$$

where $\phi \in W^{1,2}(\Omega)$. This model has the same data term as the proposed model (22):

$$E_D(f, \phi) = \lambda_1 \int_{\Omega} (f - c_1)^2 (\phi + 1)^2 dx + \lambda_2 \int_{\Omega} (f - c_2)^2 (\phi - 1)^2 dx. \quad (32)$$

For the sake of simplicity, we discuss the problem only for the case that f is an ideal binary image.

The following result shows that for an ideal binary image f , the unique global minimizer of $E_D(f, \phi)$ over $L^2(\Omega)$ is the binary step

function, which equals to 1 in the object and -1 in the background.

Theorem 5. Let f be an ideal binary image:

$$f(x) = \begin{cases} a, & x \in \omega \\ b, & x \in \Omega/\omega, a \neq b, \end{cases} \quad (33)$$

where ω and Ω/ω represent the objects of interest and the background in the image, respectively. Then we have

$$\phi^*(x) = \begin{cases} 1, & x \in \omega \\ -1, & x \in \Omega/\omega \end{cases} \quad (34)$$

is a global minimizer of $E_D(f, \phi)$.

Proof. See Appendix A.

This result is verified in Fig. 11, in which the test image f is a synthetic binary image with a rectangle object. Fig. 11(a and b) shows the surface graph of the global minimizer ϕ^* of $E_D(f, \phi)$ and

the final zero level set of ϕ^* superimposed on the original image, respectively. It can be observed from Fig. 11(a) that ϕ^* is really a binary step function, the function value being equal to 1 in the object (rectangle) and -1 in the background. The zero level set of the binary step function ϕ^* is exactly located at the edge of the rectangle object; see Fig. 11(b).

It is well known that a binary step function belongs to $L^2(\Omega)$ but not to $W^{1,2}(\Omega)$. Therefore, although the global minimizer of $E_D(f, \phi)$ over $L^2(\Omega)$ is a binary step function for an ideal binary image, it is not possible that the global minimizer of $E_{direct}(c_1, c_2, \phi)$ over $W^{1,2}(\Omega)$ still remains to be a binary step function. This may result in the case that the direct regularization model (31) cannot completely segment an ideal binary image because it requires that the level set function ϕ is within $W^{1,2}(\Omega)$. Conversely, for the indirect regularization model, we just require that the level set function ϕ is within $L^2(\Omega)$ instead of

$W^{1,2}(\Omega)$. As a result, it is possible that the global minimizer of $E(c_1, c_2, \phi, \psi)$ over $L^2(\Omega)$ with respect to ϕ still remains to be a binary step function with zero level set locating at the object edge exactly. We illustrate in Fig. 12 the effects of using direct and indirect regularization schemes (i.e., the direct model (31) and the indirect model (22)) with Algorithm I, both applied to the segmentation of a synthetic binary image with a rectangle object. The second and third columns of Fig. 12 show the final zero level sets of ϕ over the original image and the surface graphs of ϕ at steady state, respectively. It can be observed that the final level set function really remains to be the binary step function whose zero level set exactly locates at the object edge for the indirect regularization model (22), while the final level set function is not the binary step function for the direct regularization model (31), which results to the case that the rectangle edge is not extracted exactly.

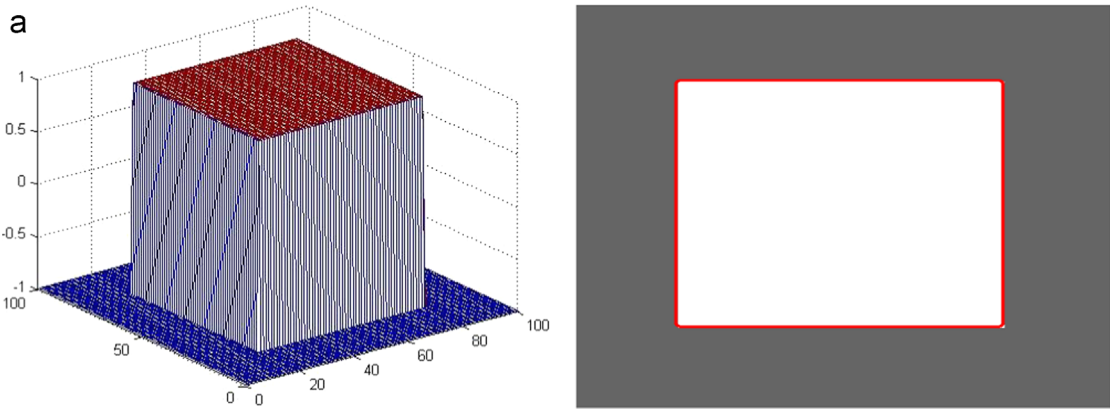


Fig. 11. Minimizer and segmentation result of $E_D(f, \phi)$ over $L^2(\Omega)$ for an ideal binary image f . (a) Surface graph of minimizer. (b) Final contour (red) superimposed on the image f . (For interpretation of the references to color in this figure legend, the reader is referred to the web version of this article.)

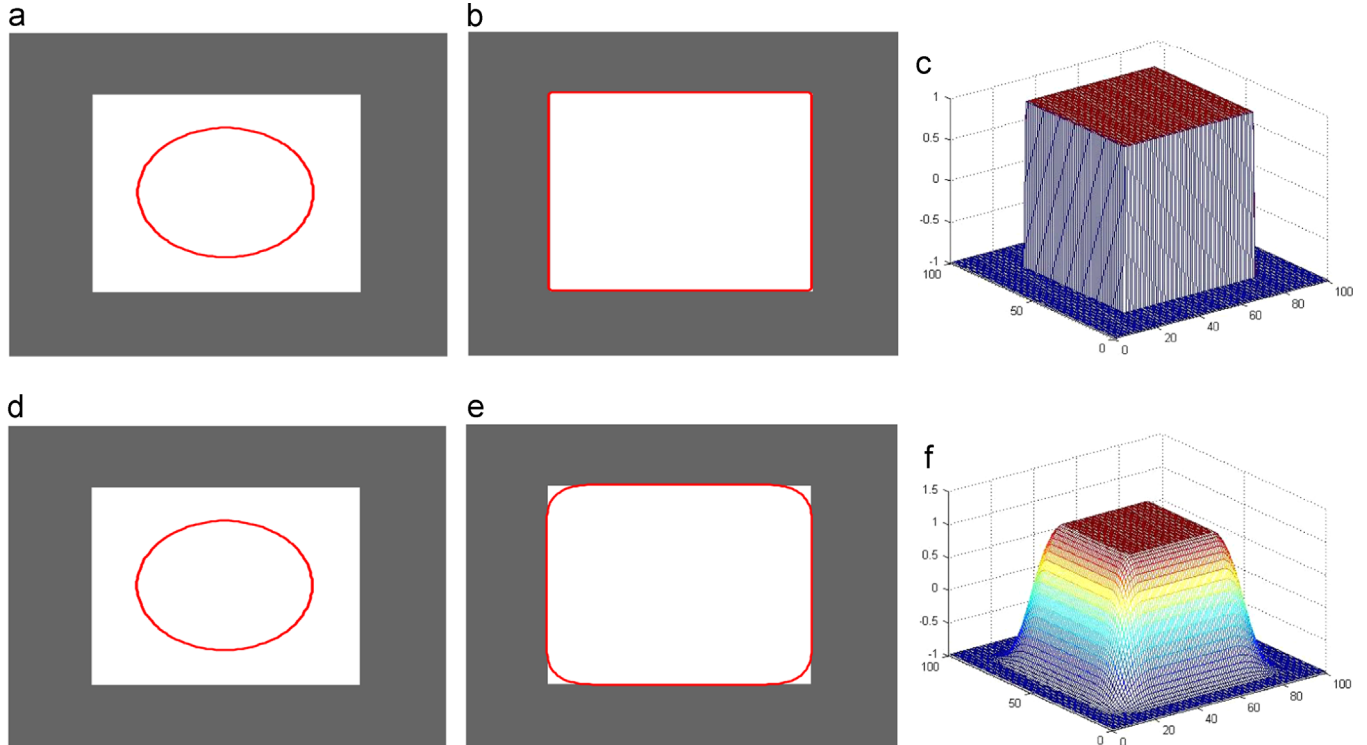


Fig. 12. Segmentation results of indirect (Top row) and direct regularization (Bottom row) methods for an ideal binary image. First column: initial contours (from signed distance functions) superimposed on the original images. Second column: segmentation results. Last column: corresponding surface graphs of final level set functions.

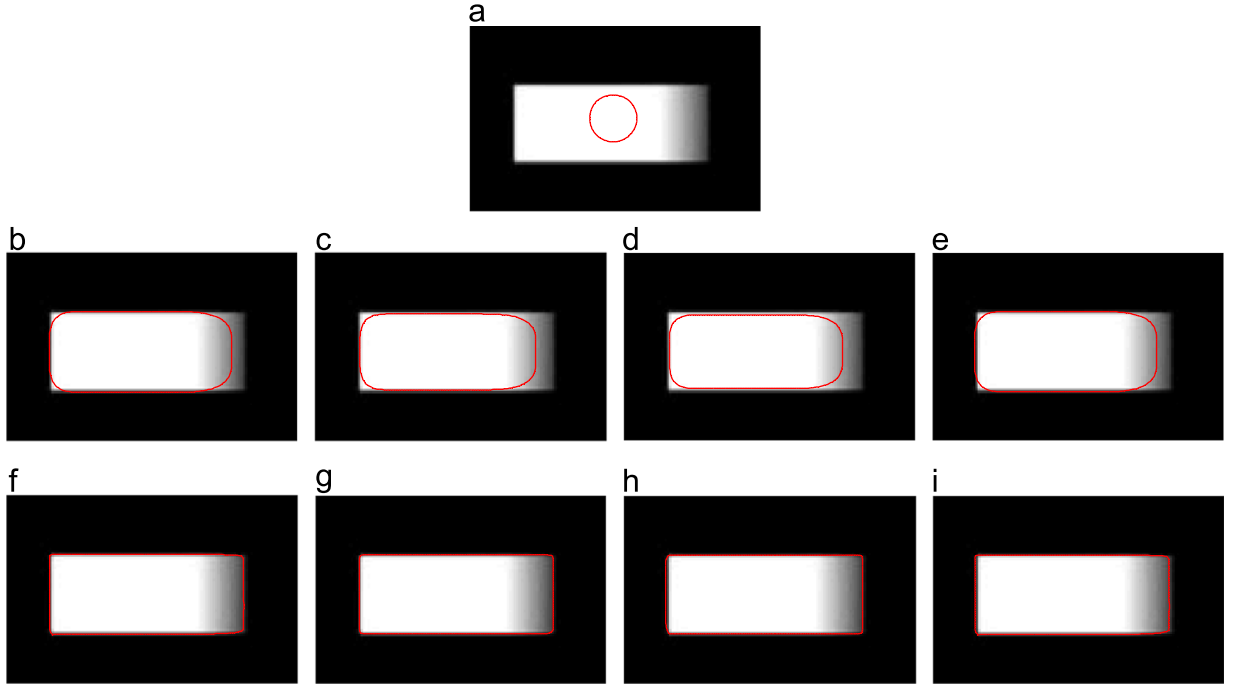


Fig. 13. Comparison of indirect and direct regularization schemes for a synthetic image with angle and weak boundary. First row: initial contour (from signed distance function) superimposed on the original image. Second row: segmentation results of direct regularization schemes (left to right: the models (35a), (36a), (37a) and (31)). Last row: segmentation results of indirect regularization schemes (left to right: the models (35b), (36b), (37b) and (22)).

On the other hand, the direct regularization model (31) regularizes directly the level set function ϕ by means of the energy $E_R(\phi) = \mu \int_{\Omega} |\nabla \phi|^2 dx$. It is obvious that the energy $E_R(\phi) = \mu \int_{\Omega} |\nabla \phi|^2 dx$ obtains the minimum only if $|\nabla \phi| = 0$. Thus, to reach the minimum of $E_R(\phi)$ using Algorithm I, we have $|\nabla \phi| \rightarrow 0$, and so the zero level set of ϕ will disappear along with the iteration process. This implies that the direct model (31) may make the zero level set of ϕ across the weak boundary, leading to boundary leakage. In contrast, the regularization of ϕ in the indirect model (22) is indirectly completed by the regularization of ψ and the link term $E_L(\phi, \psi)$. This indirect regularization scheme weakens heavily the excessive smoothness of the level set function ϕ , and so can avoid the boundary leakage.

To further test the segmentation performances of direct and indirect regularization schemes, we substitute the data terms $E_D(f, \phi)$ of the direct model (31) and the indirect model (22) by some other data terms stemming from [8–10] to obtain the following models:

$$\begin{aligned} E_{direct}^{CV}(c_1, c_2, \phi) &= \lambda_1 \int_{\Omega} (f - c_1)^2 H(\phi) dx \\ &\quad + \lambda_2 \int_{\Omega} (f - c_2)^2 (1 - H(\phi)) dx + \nu \int_{\Omega} |\nabla \phi|^2 dx, \end{aligned} \quad (35a)$$

$$\begin{aligned} E_{indirect}^{CV}(c_1, c_2, \phi, \psi) &= \lambda_1 \int_{\Omega} (f - c_1)^2 H(\phi) dx \\ &\quad + \lambda_2 \int_{\Omega} (f - c_2)^2 (1 - H(\phi)) dx \\ &\quad + \mu \int_{\Omega} (\phi - \psi)^2 dx + \nu \int_{\Omega} |\nabla \psi|^2 dx, \end{aligned} \quad (35b)$$

$$\begin{aligned} E_{direct}^{RSF}(c_1, c_2, \phi) &= \lambda_1 \iint_{\Omega} K_{\sigma}(x-y)(f(y) - f_1(x))H(\phi) dy dx \\ &\quad + \lambda_2 \iint_{\Omega} K_{\sigma}(x-y)(f(y) - f_2(x))(1 - H(\phi)) dy dx \\ &\quad + \nu \int_{\Omega} |\nabla \phi|^2 dx, \end{aligned} \quad (36a)$$

$$\begin{aligned} E_{indirect}^{RSF}(c_1, c_2, \phi, \psi) &= \lambda_1 \iint_{\Omega} K_{\sigma}(x-y)(f(y) - c_1(x))H(\phi) dy dx \\ &\quad + \lambda_2 \iint_{\Omega} K_{\sigma}(x-y)(f(y) - c_2(x))(1 - H(\phi)) dy dx \\ &\quad + \mu \int_{\Omega} (\phi - \psi)^2 dx + \nu \int_{\Omega} |\nabla \psi|^2 dx, \end{aligned} \quad (36b)$$

and

$$E_{direct}^{LIF}(\phi) = \lambda \int_{\Omega} (f - c_1(x)H(\phi) - c_2(x)(1 - H(\phi))) dx + \nu \int_{\Omega} |\nabla \phi|^2 dx, \quad (37a)$$

$$\begin{aligned} E_{indirect}^{LIF}(\phi, \psi) &= \lambda \int_{\Omega} (f - c_1(x)H(\phi) - c_2(x)(1 - H(\phi))) dx \\ &\quad + \mu \int_{\Omega} (\phi - \psi)^2 dx + \nu \int_{\Omega} |\nabla \phi|^2 dx. \end{aligned} \quad (37b)$$

In Fig. 13, we show the segmentation results of the six models (35a)–(37b) and the models (31) and (22) for a synthetic image with a rectangular object. This test image has a low contrast change near the right edge, but has still a clear discontinuity delineating the edge. For the four direct regularization schemes, no matter how to tune the parameters, the zero level set of ϕ always cuts through the low contrast region of the rectangular object (leading to boundary leak) and doesn't locate accurately the angles of the rectangular object; see the second row of Fig. 13. On the contrary, the four indirect regularization schemes all provide satisfied segmentation results, as illustrated in the third row of Fig. 13.

7. Conclusions

In this paper, we propose a new variational level set model with indirect regularization for image segmentation. We show that the indirect regularization has some advantages over direct regularization theoretically and experimentally. Experiments on synthetic and real images illustrate that the proposed model can better handle images with high noise, angle and weak edges. The indirect regularization scheme can be easily combined with data

terms of some existing variational models so that new models to better handle with high noise, angle and weak edges. In the future work, we will investigate the indirect regularization scheme to handle with texture images by combining with data terms of some other existing variational models.

Acknowledgments

This work was partially supported by the Chinese National Science Foundation (NSFC11371384 and NSFC61202349), the Nature Science Foundation Project of CQCSTC (cstc2013jcyja40058), and Chongqing Graduate Student Research Innovation Projects (Grant no. CYB14002 and CYS14020). The authors gratefully thank the anonymous reviewers for their valuable comments and suggestions.

Appendix A

Proof of Theorem 1

Proof. Fix $c_1 = c_1^*$ and $c_2 = c_2^*$, $\forall a, b > 0$ with $a+b=1$. For any $(\phi_1, \psi_1), (\phi_2, \psi_2) \in L^2(\Omega) \times W^{1,2}(\Omega)$, we have

$$\begin{aligned} (a\phi_1 + b\phi_2 + 1)^2 &= (a(\phi_1 + 1) + b(\phi_2 + 1))^2 \\ &= a^2(\phi_1 + 1)^2 + b^2(\phi_2 + 1)^2 + 2ab(\phi_1 + 1)(\phi_2 + 1) \\ &\leq a^2(\phi_1 + 1)^2 + b^2(\phi_2 + 1)^2 \\ &\quad + ab((\phi_1 + 1)^2 + (\phi_2 + 1)^2) \\ &= a(a+b)(\phi_1 + 1)^2 + b(b+a)(\phi_2 + 1)^2 \\ &= a(\phi_1 + 1)^2 + b(\phi_2 + 1)^2. \end{aligned} \quad (\text{A.1})$$

Similarly,

$$\begin{aligned} (a\phi_1 + b\phi_2 - 1)^2 &= (a(\phi_1 - 1) + b(\phi_2 - 1))^2 \\ &\leq a(\phi_1 - 1)^2 + b(\phi_2 - 1)^2. \end{aligned} \quad (\text{A.2})$$

For the third term, we have

$$\begin{aligned} (a\phi_1 + b\phi_2 - a\psi_1 - b\psi_2)^2 &= (a(\phi_1 - \psi_1) + b(\phi_2 - \psi_2))^2 \\ &= a^2(\phi_1 - \psi_1)^2 + b^2(\phi_2 - \psi_2)^2 + 2ab(\phi_1 - \psi_1)(\phi_2 - \psi_2) \\ &\leq a^2(\phi_1 - \psi_1)^2 + b^2(\phi_2 - \psi_2)^2 + ab((\phi_1 - \psi_1)^2 + (\phi_2 - \psi_2)^2) \\ &= a(\phi_1 - \psi_1)^2 + b(\phi_2 - \psi_2)^2. \end{aligned} \quad (\text{A.3})$$

As for the gradient regularized term, we have the following conclusion:

$$\begin{aligned} |\nabla(a\psi_1 + b\psi_2)|^2 &= |a\nabla\psi_1 + b\nabla\psi_2|^2 \\ &= a^2|\nabla\psi_1|^2 + b^2|\nabla\psi_2|^2 + 2ab|\nabla\psi_1||\nabla\psi_2| \\ &\leq a|\nabla\psi_1|^2 + b|\nabla\psi_2|^2. \end{aligned} \quad (\text{A.4})$$

Using (A.1)–(A.4), we get

$$E(c_1^*, c_2^*, a\phi_1 + b\phi_2, a\psi_1 + b\psi_2) \leq aE(c_1^*, c_2^*, \phi_1, \psi_1) + bE(c_1^*, c_2^*, \phi_2, \psi_2).$$

Thus, the energy functional is convex. This completes the proof.

Proof of Theorem 2

Proof. Let $c_1 = c_1^*$, $c_2 = c_2^*$ and $\psi = \psi^* \in W^{1,2}(\Omega)$.

First, we prove that $E(c_1^*, c_2^*, \phi, \psi^*)$ is a nonnegative and proper function with respect to ϕ , namely

$$0 \leq \inf_{\phi \in L^2(\Omega)} E(c_1^*, c_2^*, \phi, \psi^*) < \infty.$$

In fact, the left inequality is obvious. Moreover, since $0 \in L^2(\Omega)$ we have

$$\begin{aligned} &\inf_{\phi \in L^2(\Omega)} E(c_1^*, c_2^*, \phi, \psi^*) \\ &\leq E(c_1^*, c_2^*, 0, \psi^*) \\ &= \lambda_1 \int_{\Omega} (f - c_1^*)^2 dx + \lambda_2 \int_{\Omega} (f - c_2^*)^2 dx \\ &\quad + \mu \int_{\Omega} |\psi^*|^2 dx + \nu \int_{\Omega} |\nabla \psi^*|^2 dx < \infty. \end{aligned}$$

Then, we show that $E(c_1^*, c_2^*, \phi, \psi^*)$ is coercive on $L^2(\Omega)$. In fact, it easily follows that

$$\begin{aligned} \|\phi\|_2 &= \|\phi - \psi^* + \psi^*\|_2 \\ &\leq \|\phi - \psi^*\|_2 + \|\psi^*\|_2 \\ &\leq \sqrt{\frac{1}{\mu} E(c_1^*, c_2^*, \phi, \psi^*) + \|\psi^*\|_2^2}, \end{aligned}$$

which implies that

$$\lim_{\|\phi\|_2 \rightarrow \infty} E(c_1^*, c_2^*, \phi, \psi^*) = \infty.$$

The coerciveness of $E(c_1^*, c_2^*, \phi, \psi^*)$ on $L^2(\Omega)$ is thus proved.

Finally, we prove that $E(c_1^*, c_2^*, \phi, \psi^*)$ has a unique minimizer $\phi^* \in L^2(\Omega)$. In fact, we know from Theorem 1 that $E(c_1^*, c_2^*, \phi, \psi^*)$ is convex and so lower semi-continuous with respect to ϕ . Note that $L^2(\Omega)$ is a reflective Banach space. Using the proposition 1.2 in [27], $E(c_1^*, c_2^*, \phi, \psi^*)$ has a unique minimizer $\phi^* \in L^2(\Omega)$.

Let $c_1 = c_1^*$, $c_2 = c_2^*$ and $\phi = \phi^* \in L^2(\Omega)$.

First we prove that $E(c_1^*, c_2^*, \phi^*, \psi)$ is a nonnegative and proper function with respect to ψ , i.e.,

$$0 \leq \inf_{\psi \in W^{1,2}(\Omega)} E(c_1^*, c_2^*, \phi^*, \psi) < \infty.$$

In fact, the left inequality is obvious. Moreover, since $0 \in W^{1,2}(\Omega)$ we obtain

$$\begin{aligned} &\inf_{\psi \in W^{1,2}(\Omega)} E(c_1^*, c_2^*, \phi^*, \psi) \\ &\leq E(c_1^*, c_2^*, \phi^*, 0) \\ &= \lambda_1 \int_{\Omega} (f - c_1^*)^2 (\phi^* + 1)^2 dx + \lambda_2 \int_{\Omega} (f - c_2^*)^2 (\phi^* + 1)^2 dx \\ &\quad + \mu \int_{\Omega} |\phi^*|^2 dx < \infty. \end{aligned}$$

Then we prove the existence of minimizer of $E(c_1^*, c_2^*, \phi^*, \psi)$. Note that $W^{1,2}(\Omega)$ is a reflective Banach space, and we know from Theorem 1 that $E(c_1^*, c_2^*, \phi^*, \psi)$ is convex and thus lower semi-continuous. Using the proposition 1.2 in [27], we just to prove that $E(c_1^*, c_2^*, \phi^*, \psi)$ is coercive on $W^{1,2}(\Omega)$. The coercive of $E(c_1^*, c_2^*, \phi^*, \psi)$ can be given by

$$\begin{aligned} \|\psi\|_2 &= \|\psi - \phi^* + \phi^*\|_2 \\ &\leq \|\phi^* - \psi\|_2 + \|\phi^*\|_2 \\ &\leq \sqrt{\frac{1}{\mu} E(c_1^*, c_2^*, \phi^*, \psi) + \|\phi^*\|_2^2} \end{aligned} \quad (\text{A.5})$$

and

$$\begin{aligned} \|\nabla \psi\|_2 &= \left(\int_{\Omega} |\nabla \psi|^2 dx \right)^{\frac{1}{2}} \\ &\leq \sqrt{\frac{1}{\nu} E(c_1^*, c_2^*, \phi^*, \psi)}. \end{aligned} \quad (\text{A.6})$$

In fact, using (A.5) and (A.6), we have

$$\|\psi\|_{1,2} = \|\psi\|_2 + \|\nabla \psi\|_2$$

$$\leq \sqrt{\frac{1}{\mu} + \frac{1}{\nu}} \sqrt{E(c_1^*, c_2^*, \phi^*, \psi)} + \|\phi^*\|_2,$$

which implies that

$$\lim_{\|\psi\|_1 \rightarrow \infty} E(c_1^*, c_2^*, \phi^*, \psi) = \infty.$$

This means that $E(c_1^*, c_2^*, \phi^*, \psi)$ is coercive on $W^{1,2}(\Omega)$. Moreover, since $E(c_1^*, c_2^*, \phi^*, \psi)$ is strictly convex, it has a unique minimizer $\psi^* \in W^{1,2}(\Omega)$. This completes the proof.

Proof of Theorem 3

Proof. Using (27), it is easily verified that

$$\begin{aligned} E(c^{k+1}, \phi^{k+1}, \psi^{k+1}) &\leq E(c^k, \phi^{k+1}, \psi^{k+1}) \\ &\leq E(c^k, \phi^{k+1}, \psi^k) \\ &\leq E(c^k, \phi^k, \psi^k) \\ &\leq E(c^{k-1}, \phi^k, \psi^k) \\ &\leq E(c^{k-1}, \phi^k, \psi^{k-1}). \end{aligned}$$

Since $E(c, \phi, \psi)$ is bounded from below (due to $E(c, \phi, \psi) \geq 0$), the sequence $\{E(c^k, \phi^k, \psi^k)\}_{k \in \mathbb{N}}$ converges monotonically. This completes the proof. \square

Proof of Theorem 4

Proof. Using (27), for each k , we have

$$E(c^k, \phi^k, \psi^k) \leq E(c, \phi^k, \psi^k), \quad \forall c \in \mathbb{R}^2.$$

By the continuity of $E(\cdot, \cdot, \cdot)$, we obtain, as $k \rightarrow \infty$,

$$E(c^*, \phi^*, \psi^*) \leq E(c, \phi^*, \psi^*), \quad \forall c \in \mathbb{R}^2.$$

On the other hand, for each k , we have for any,

$$\begin{aligned} E(c^k, \phi^k, \psi^k) &\leq E(c^{k-1}, \phi^k, \psi^k) \\ &\leq E(c^{k-1}, \phi^k, \psi^{k-1}) \quad \forall \phi \in L^2(\Omega) \\ &\leq E(c^{k-1}, \phi, \psi^{k-1}), \end{aligned}$$

and

$$E(c^k, \phi^k, \psi^k) \leq E(c^{k-1}, \phi^k, \psi^k) \leq E(c^{k-1}, \phi^k, \psi), \quad \forall \psi \in W^{1,2}(\Omega)$$

Combining with the continuity of $E(\cdot, \cdot, \cdot)$, we have, as $k \rightarrow \infty$,

$$E(c^*, \phi^*, \psi^*) \leq E(c^*, \phi, \psi^*), \quad \forall \phi \in L^2(\Omega),$$

and

$$E(c^*, \phi^*, \psi^*) \leq E(c^*, \phi^*, \psi), \quad \forall \psi \in W^{1,2}(\Omega)$$

This completes the proof.

Proof of Theorem 5

Proof. By (23), we have

$$\begin{aligned} c_1 &= \frac{\int_{\Omega} f(x) (\phi^*(x) + 1)^2 dx}{\int_{\Omega} (\phi^*(x) + 1)^2 dx} \\ &= \frac{\int_{\omega} f(x) (\phi^*(x) + 1)^2 dx + \int_{\Omega \setminus \omega} f(x) (\phi^*(x) + 1)^2 dx}{\int_{\omega} (\phi^*(x) + 1)^2 dx + \int_{\Omega \setminus \omega} (\phi^*(x) + 1)^2 dx} \end{aligned}$$

$$= \frac{\int_{\omega} 4ad\mathbf{x} + 0}{\int_{\omega} 4d\mathbf{x} + 0} = a. \quad (\text{A.7})$$

Similarly,

$$c_2 = \frac{\int_{\Omega} f(x) (\phi^*(x) + 1)^2 dx}{\int_{\Omega} (\phi^*(x) - 1)^2 dx} = b. \quad (\text{A.8})$$

Thus, we have

$$\begin{aligned} E_D(f, \phi^*) &= \lambda_1 \int_{\Omega} (f(x) - c_1)^2 (\phi^*(x) + 1)^2 dx \\ &\quad + \lambda_2 \int_{\Omega} (f(x) - c_2)^2 (\phi^*(x) - 1)^2 dx \\ &= \lambda_1 \int_{\Omega \setminus \omega} (b - a)^2 (-1 + 1)^2 dx + \lambda_2 \int_{\omega} (a - b)^2 (1 - 1)^2 dx \\ &= 0. \end{aligned}$$

Since $E_D(f, \phi) \geq 0$ for any $\phi \in L^2(\Omega)$, we have $\phi^* = \arg \min_{\phi \in L^2(\Omega)} E(\phi)$. This completes the proof.

References

- [1] N. Paragios, R. Deriche, Geodesic active regions and level set methods for supervised texture segmentation, *Int. J. Comput. Vis.* 46 (3) (2002) 223–247.
- [2] K. Zhang, L. Zhang, H. Song, W. Zhou, Active contours with selective local or global segmentation: a new formulation and level set method, *Image Vision Comput.* 28 (4) (2010) 668–676.
- [3] Y. Wang, C. He, Adaptive level set evolution starting with a constant function, *Appl. Math. Model.* 36 (2012) 3217–3228.
- [4] Y. Yuan, C. He, Adaptive active contours without edges, *Math. Comput. Modell.* 55 (2012) 1705–1721.
- [5] K. Zhang, L. Zhang, H. Song, D. Zhang, Re-initialization free level set evolution via reaction diffusion, *IEEE Trans. Image Process.* 22 (1) (2013) 258–271.
- [6] S. Taheri, S. Ong, V. Chong, Level-set segmentation of brain tumors using a threshold-based speed function, *Image Vision Comput.* 28 (1) (2010) 26–37.
- [7] S. Balla-Arabé, X. Gao, B. Wang, F. Yang, V. Brost, Multi-kernel implicit curve evolution for selected texture region segmentation in VHR satellite images, *IEEE Trans. Geosci. Remote Sens.* 52 (8) (2014) 5183–5192.
- [8] T. Chan, L. Vese, Active contours without edges, *IEEE Trans. Image Process.* 10 (2) (2001) 266–277.
- [9] C. Li, C. Kao, J. Gore, Z. Ding, Minimization of region-scalable fitting energy for image segmentation, *IEEE Trans. Image Process.* 17 (10) (2008) 1940–1949.
- [10] K. Zhang, H. Song, L. Zhang, Active contours driven by local image fitting energy, *Pattern Recognit.* 43 (2010) 1199–1206.
- [11] C. Li, R. Huang, Z. Ding, et al., A level set method for image segmentation in the presence of intensity inhomogeneities with application to MRI, *IEEE Trans. Image Process.* 20 (7) (2011) 2007–2016.
- [12] Y. Chen, J. Zhang, A. Mishra, J. Yang, Image segmentation and bias correction via an improved level set method, *Neurocomputing* 74 (17) (2011) 3520–3530.
- [13] T. Chan, S. Glu, M. Nikolova, Algorithms for finding global minimizers of image segmentation and denoising models, *SIAM J. Appl. Math.* 66 (5) (2006) 1632–1648.
- [14] X. Bresson, S. Esedoglu, P. Vandergheynst, S. Osher, Fast global minimization of the active contour/snake model, *J. Math. Imaging Vis.* 28 (2007) 151–167.
- [15] E. Brown, T. Chan, X. Bresson, Completely convex formulation of the Chan-Vese image segmentation model, *Int. J. Comput. Vis.* 98 (1) (2012) 103–121.
- [16] Y. Wu, C. He, A convex variational level set model for image segmentation, *Signal Process.* 106 (2015) 123–133.
- [17] S. Lee, J. Seo, Level set-based bimodal segmentation with stationary global minimum, *IEEE Trans. Image Process.* 15 (2006) 2843–2852.
- [18] Y. Li, J. Kim, An unconditionally stable numerical method for bimodal image segmentation, *Appl. Math. Comput.* 219 (2012) 3083–3090.
- [19] S. Balla-Arabé, X. Gao, B. Wang, A fast and robust level set method for image segmentation using fuzzy clustering and lattice Boltzmann method, *IEEE Trans. Cybern.* 43 (3) (2013) 910–920.
- [20] C. Li, C. Xu, C. Gui, M. Fox, Level set evolution without re-initialization: a new variational formulation. In: Proc. IEEE Conf. Comput. Vis. Pattern Recognit. 1 (2005) pp. 430–436.
- [21] C. Li, C. Xu, C. Gui, M. Fox, Distance regularized level set evolution and its application to image segmentation, *IEEE Trans. Image Process.* 19 (12) (2010) 154–164.
- [22] X. Xie, Active contouring based on gradient vector interaction and constrained level set diffusion, *IEEE Trans. Image Process.* 19 (1) (2010) 154–164.
- [23] X. Wang, J. Shan, Y. Niu, L. Tan, S. Zhang, Enhanced distance regularization for re-initialization free level set evolution with application to image segmentation, *Neurocomputing* 141 (2014) 223–235.
- [24] D. Cremers, S. Osher, S. Soatto, Kernel density estimation and intrinsic alignment for shape priors in level set segmentation, *Int. J. Comput. Vis.* 69 (3) (2006) 335–351.

- [25] B. Wang, X. Gao, J. Li, X. Li, D. Tao, A Level Set with Shape Priors Using Moment-based Alignment and Locality Preserving Projections, IScIDE, LNCS 8261, 2013, pp. 697–704.
- [26] P. Tseng, Applications of splitting algorithm to decomposition in convex programming and variational inequalities, SIAM J. Control Optim. 29 (1991) 119–138.
- [27] I. Ekeland, R. Temam, Convex Analysis and Variational Problem, SIAM, Philadelphia, 1999.
- [28] Y. Wang, J. Yang, W. Yin, Y. Zhang, A new alternating minimization algorithm for total variation image reconstruction, SIAM J. Imag. Sci. 1 (3) (2008) 248–272.
- [29] X. Tai, J. Hahn, G. Chung, A fast algorithm for Euler's elastic model using augmented Lagrangian method, SIAM J. Imag. Sci. 4 (1) (2011) 313–344.
- [30] T. Chan, J. Shen, Image Processing and Analysis: Variational, PDE, Wavelet, and Stochastic Methods, SIAM, Philadelphia, PA, 2005.
- [31] R. Crandall, Image Segmentation Using the Chan–Vese Algorithm. Project Report from ECE 532, Fall, 2009 .
- [32] B. Liu, H. Cheng, J. Huang, J. Tian, et al., Probability density difference-based active contour for ultrasound image segmentation, Pattern Recognit. 43 (6) (2010) 2028–2042.
- [33] D. Shattuck, S. Sandor, K. Schaper, et al., Magnetic resonance image tissue classification using a partial volume model, NeurolImage 13 (5) (2001) 856–876.
- [34] D. Martin, C. Fowlkes, D. Tal, J. Malik, A database of human segmented natural images and its application to evaluating segmentation algorithms and measuring ecological statistics, In: Proc. IEEE int. Conf. comp. vis. 2, 2001, pp. 416–423.



Chuanjiang He received the BS degree in pure mathematics and the MS degree in applied mathematics from Sichuan University, Chengdu, China, in 1985 and 1988, respectively, and the PhD degree in control theory and control engineering from Chongqing University, Chongqing, China, in 2004. From March 1995 to August 2005, he was an assistant professor in the Department of Mathematics, Chongqing University. Since September 2005, he has been a professor in the Department of Information and Computing Science, Chongqing University. His research interests include partial differential equations and image processing, etc.



Yongfei Wu received the MS degree in Applied Mathematics from Chongqing University, Chongqing, China, in 2013. Currently, he is a PhD candidate, the Department of Information and Computing Science, Chongqing University. His research interests include variational methods and partial differential equations for image processing, etc.